Proceedings of the Thirty-fifth (2025) International Ocean and Polar Engineering Conference **www.isope.org**
Seoul/Goyang, Korea, June 1-6, 2025

ISBN 978-1-880653-74-6; ISSN 1098-6189

Correlation Between Material Certificate Data and Damage Mechanics Parameters in the Upper-Shelf Regime for S690Q Steels

Wei Jun Wong, Carey L. Walters
Department of Maritime and Transport Technology,
Delft University of Technology, South Holland, the Netherlands

ABSTRACT

Calibration of ductile damage models typically involves significant experimental and reverse engineering effort, due to their stress-state dependent nature. Having access to the calibrated damage parameters for a range of materials could enable finite-element analyses of the fracture performance of the different materials in a structural detail and aid in material selection based on specific criteria such as the ductility or the toughness of the detail. By performing a parametric study and regression analysis using a previously validated rate- and temperature-dependent damage-plasticity model, considering steels with a yield strength between 730 MPa and 850 MPa, this paper presents correlations between easily available material certificate properties and calibrated damage model parameters, developed for the purpose of modelling the standardised single-edge notched bending (SENB) crack-tip opening displacement (CTOD) fracture toughness test. First, the correlations provide a tool for quickly estimating the calibrated parameters for the type of material considered in the study, so that damage mechanics modelling can be used in subsequent parametric investigations and design considerations concerning SENB fracture toughness testing. Second, the correlations give insight into the trends and relative importance of the plasticity and damage parameters in relation to the variations in engineering properties from the widely used tensile test and Charpy test, which are the fracture elongation A and Charpy energy C_v, respectively. By relating the properties obtained from these tests, which involve known stress states at key locations in the test specimens, to the strains in stress-state-dependent damage initiation locus, physical insight is obtained regarding the role of the normalised damage parameters, which are the damage initiation strains. Such information is useful both for understanding how plasticity parameters are related to fracture toughness and for the future calibration of similar materials. Finally, it is found that parametrically varying the yield strength σ_y and the yield-to-tensile strength ratio σ_y/σ_u simultaneously according to observed empirical trends has a small effect on the correlations between notch toughness and damage initiation strains when compared to the significantly larger effect of A. Since the damage initiation strains are directly correlated to the fracture behaviour, the σ_y/σ_u ratio's small influence suggests that it might not be a good choice as a local ductility indicator for a material in terms of ductile fracture, although it is so used in practice, a point which remains to be ascertained through further study of fracture toughness testing and simulation in light of the present findings. By the same token, the existing correlations between C_v and fracture toughness, which have not taken the effect of variations in A and σ_y/σ_u into account, should be reconsidered in light of these effects.

KEY WORDS: High-strength steels; mill test report; modified Mohr-Coulomb; notch energy; strain rate; tensile test; thermal softening

INTRODUCTION

Calibration of phenomenological ductile damage models usually involves significant experimental and inverse engineering effort, due to the stress-state dependent nature of damage behaviour. For example, the widely used uncoupled modified Mohr-Coulomb (MMC; Bai and Wierzbicki, 2010) and Hosford-Coulomb (Mohr and Marcadet, 2015) models each have three parameters describing the damage strain locus and are typically calibrated with at least three different characterisation tests, using specimens which induce specific stress states, such as the butterfly, notched, grooved or punch specimens. Often, calibration involves performing these tests with instrumentation adequate for quantifying local strains, such as digital image correlation, and detailed finite-element modelling to simulate the observed strains. Furthermore, when coupled damage-plasticity with material softening is considered, additional testing is typically required to characterise the softening behaviour (Cao, 2015).

The calibration effort involved in characterising a given material constitutes a barrier to the use of these models in design considerations. For example, having access to the calibrated damage parameters for a range of materials could aid in material choice in structural design based on specific criteria, such as the ductility of a component or the toughness of a detail, by enabling finite-element analyses of the fracture performance of the different materials in the component or detail.

By performing a parametric study and regression analysis using a previously validated rate- and temperature-dependent damage-plasticity model, considering steels with a yield strength between 730 MPa and 850 MPa, this paper presents correlations between easily available material certificate properties and calibrated damage model parameters, developed for the purpose of modelling the standardised single-edge notched bending (SENB) crack-tip opening displacement (CTOD) fracture toughness test. Besides providing a tool for estimating the calibrated damage parameters for the subsequent modelling of CTOD tests (which is outside the scope of this paper), this study gives insight into the role and the relative importance of the damage locus parameters and sheds light on the coupling effects between plasticity, as represented by the yield-to-tensile strength ratio, and damage, as represented by the damage parameters.

This regression-based calibration of a range of materials with varying properties is largely enabled by the reduced calibration effort due to the assumption of triaxiality independence and a two-parameter calibration approach, which has been shown by the present authors (Wong and Walters, 2025) to work well for steels with weak triaxiality dependence in the fracture locus in the medium-to-high triaxiality range, a notion supported by observations made by Xue (2009, 2010) on existing experiments on structural steels (Clausing, 1970) and aluminium alloy (Banabic et al., 2005). Additionally, known theoretical relationships and empirical relationships specific to S690 steel in the literature concerning plasticity, rate-effects and thermal effects are adopted, as described in the sections below. Similarities in the stress state distributions observed in key stages of the Charpy and CTOD tests provide the grounds for the application of the calibration correlation to CTOD modelling (Wong and Walters, 2025). Due to these assumptions, it is important to note that the following findings are not suitable to be extrapolated for application to other structural details, steels which are strongly triaxiality dependent or steel grades which are not similar to S690. Besides its use within the range of applicability, these correlations provide useful generalisable insight into the correlations between damage parameters, plasticity parameters and engineering properties from the material certificate data.

RATE- AND TEMPERATURE-DEPENDENT DAMAGE-SOFTENING PLASTICITY MODEL

A rate- and temperature-dependent damage-softening flow plasticity model, as described by Wong and Walters (2025), is used. The effects are coupled multiplicatively in the yield function shown in Eq. 1, which is solved by using the consistency viscoplasticity formulation by Wang et al. (1997).

$$f = \sigma_v - \bar{\sigma} R \beta X \tag{1}$$

where f is the yield function; σ_v is the von Mises equivalent stress; $\bar{\sigma}$ is the plastic strain-hardening stress; R is the rate-dependence factor; β is the softening coefficient; and X is the thermal softening factor.

Plasticity

The plastic strain-hardening stress $\bar{\sigma}$ is described by a Swift-type (1952) stress-strain curve combined with a yield plateau:

$$\bar{\sigma} = \begin{cases} \sigma_y \left(\dfrac{\varepsilon_{sh} - \dfrac{\sigma_y}{E}}{\varepsilon_{sh,p}} \varepsilon_p + \dfrac{\sigma_y}{E} + 1 \right) & 0 < \varepsilon_p < \varepsilon_{sh,p} \\ K(\varepsilon_p - \varepsilon_0)^n & \varepsilon_p \geq \varepsilon_{sh,p} \end{cases} \tag{2}$$

$$\varepsilon_{sh,p} = \ln(1 + \varepsilon_{sh}) - \ln\left(1 + \frac{\sigma_y}{E}\right) \tag{3}$$

where ε_p is the true equivalent plastic strain; ε_{sh} and $\varepsilon_{sh,p}$ are respectively the total engineering strain and the true equivalent plastic strain corresponding to the end of the yield plateau; K is the strength coefficient; n is the strain hardening exponent; and ε_0 is the Swift offset parameter.

In the present simulations, the σ_y and σ_u are obtained directly from the material certificate. The Young's modulus E, which is very similar for most structural steels, is here assumed to be 200 GPa (together with a Poisson's ratio of 0.3). The ε_{sh} and ε_u are obtained from the relationships proposed by Yun and Gardner (2017), derived from from regression analysis of 455 engineering stress-strain curves of structural hot-rolled steels with nominal grades up to S690, as shown in Eqs. 4 and 5:

$$\varepsilon_{sh} = \begin{cases} 0.0015 & \frac{\sigma_y}{\sigma_u} < 0.7 \\ 0.1\dfrac{\sigma_y}{\sigma_u} - 0.055 & 0.7 \leq \frac{\sigma_y}{\sigma_u} \leq 0.85 \\ 0.03 & \frac{\sigma_y}{\sigma_u} > 0.85 \end{cases} \tag{4}$$

$$\varepsilon_u = \begin{cases} 0.6\left(1 - \frac{\sigma_y}{\sigma_u}\right) & \frac{\sigma_y}{\sigma_u} \leq 0.9 \\ 0.06 & \frac{\sigma_y}{\sigma_u} > 0.9 \end{cases} \tag{5}$$

Given the known values above, assuming that the occurrence of the ultimate tensile strength σ_u and the associated uniform elongation ε_u satisfies the Considère (1885) criterion for necking and that the Swift power hardening curve intersects the yield plateau at $\varepsilon_p = \varepsilon_{sh,p}$ enables the remaining parameters K, n, ε_0 to be solved for. Thus, an estimate of the plastic strain hardening curve can be found from the σ_y and σ_u available from a material certificate.

Strain-rate dependence

The rate-dependence factor R is described by a Cowper-Symonds-type (1957) relation:

$$R = 1 - \left(\frac{\dot{\varepsilon}_{p,uni} + \dot{\varepsilon}_{p0}}{C}\right)^{\frac{1}{q}} + \left(\frac{\dot{\varepsilon}_p + \dot{\varepsilon}_{p0}}{C}\right)^{\frac{1}{q}} \tag{6}$$

where C is the Cowper-Symonds coefficient; and q is the Cowper-Symonds exponent; $\dot{\varepsilon}_p$ is the equivalent plastic strain rate; $\dot{\varepsilon}_{p,uni}$ is the quasi-static-uniaxial-testing equivalent plastic strain rate; and $\dot{\varepsilon}_{p0}$ is the equivalent plastic strain rate offset parameter which serves to ensure that the gradient of R with respect to $\dot{\varepsilon}_p$ is finite when $\dot{\varepsilon}_p = 0$ as needed for convergence in the solution of the yield function (Eq. 1), unlike in the original Cowper-Symonds equation where it is infinite.

Both the $\dot{\varepsilon}_{p,uni}$ and $\dot{\varepsilon}_{p0}$ are here assumed to be $0.000\,25\ \mathrm{s}^{-1}$, the uniaxial testing rate according to ISO 6892-1 (ISO, 2019). C and q are assumed to be $40\,524.5\ \mathrm{s}^{-1}$ and 3.3, respectively, based on least-squares fitting

to existing experimental data in the literature (Alabi et al., 2018; Yang et al., 2019, 2020; Huo et al., 2022), as shown in Fig. 1. The data from Dong et al. (2022) was not included in the fit due to its nature as an outlier in comparison to the data cloud formed by the rest of the experiments.

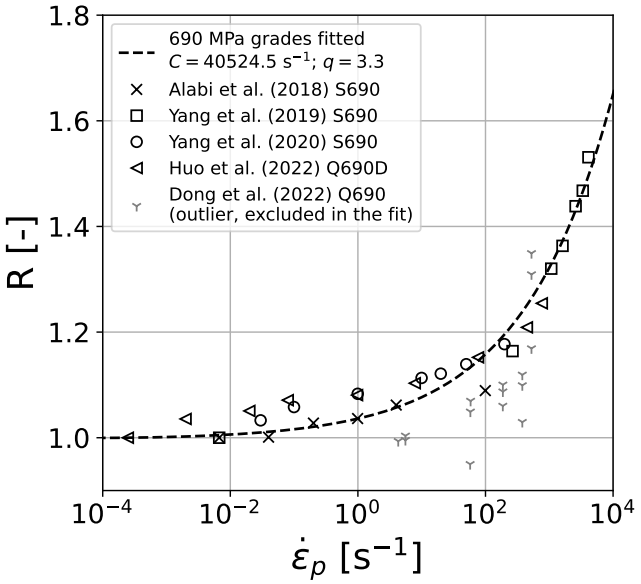

Fig. 1 Least-squares fit of R and experiments in the literature (Alabi et al., 2018; Yang et al., 2019, 2020; Huo et al., 2022; Dong et al., 2022).

Thermal softening

The thermal softening factor X is based on that of the Johnson-Cook (1985) plasticity model:

$$X = 1 - \left(\frac{\Theta - \Theta_r}{\Theta_m - \Theta_r} \right)^{m_x} \tag{7}$$

where Θ is the temperature, Θ_m is the melting temperature, Θ_r is the room temperature, and m_x is the thermal softening exponent.

In the Charpy simulations, in which accounting for thermal softening effects is important (Tanguy et al., 2005; Seo et al., 2024) especially when the Charpy impact energy C_v is high (Wong and Walters, 2025), adiabatic conditions are assumed, such that the energy dissipated due to plastic deformation leads to an increase in the temperature of the material, according to the relationships given in Eqs. 8 and 9:

$$\dot{\mathcal{D}}_p = \frac{\boldsymbol{\sigma} : \dot{\boldsymbol{\varepsilon}}_{\boldsymbol{vp}}}{\rho} \tag{8}$$

where $\dot{\mathcal{D}}_p$ is the rate of internal work done attributed to plastic deformation (Besseling and van der Giessen, 1994); $\boldsymbol{\sigma}$ is the Cauchy stress tensor, $\dot{\boldsymbol{\varepsilon}}_{\boldsymbol{vp}}$ is the viscoplastic strain rate tensor, and ρ is the density of the material.

The rate of temperature increase is calculated from:

$$\dot{\Theta} = \frac{\chi \dot{\mathcal{D}}_p}{c} \tag{9}$$

where χ is the proportion of the plastic dissipation energy converted to heat (Taylor and Quinney, 1933); and c is the specific heat capacity of the material.

In this study, the density ρ of the steel is assumed to be $7850\,\mathrm{kg\,m^{-3}}$; χ is assumed to be 0.9, as proposed by Meyers (1994); and Θ_m, Θ_r, m_x and c are assumed to be 1527 °C, 20 °C, 1.071 and $452\,\mathrm{J\,kg^{-1}\,°C^{-1}}$, respectively, as given by Dey et al. (2004) for Weldox 700 E steel, which is graded as S690QL (CEN, 2019). The simulations of the quasi-static tension test are assumed to be isothermal, with X (Eq. 7) always equal to one.

Damage

The damage-softening coefficient β is described by the model of Li and Wierzbicki (2010), as given in Eq. 10:

$$\beta = \begin{cases} 1 & D \leq 1 \\ \left(\dfrac{D_c - D}{D_c - 1} \right)^m & 1 < D < D_c \\ 0 & D = D_c \end{cases} \tag{10}$$

where D is the damage indicator; D_c is the critical damage at which the strength is fully degraded to 0; and m is the damage softening exponent.

In this study, linearity is assumed for the softening behaviour with respect to D, such that $m = 1$. A D_c of 1.3 is assumed, based on calibrations of the present model to S690QL and AH36 steel by Wong and Walters (2025) together with the observation that similar types of steels from different studies have similar D_c: 2.1–2.3 for low-alloy steel pipes (Sakonder et al., 2022), 1.2–1.4 for nickel-chromium Inconel alloy (Sarzosa et al., 2022; Algarni et al., 2015) and 1.2–1.3 for hot-rolled low carbon structural steel (Wong and Walters, 2025; Chen et al., 2023).

The damage D builds up according to the accumulation of incremental equivalent plastic strains relative to the stress-state-dependent instantaneous damage initiation strain ε_f, as described by Eqs. 11 and 12, the strain-based formulation of the modified Mohr-Coulomb (MMC) model (Bai and Wierzbicki, 2010).

$$D = \int_0^{\varepsilon_p} \frac{1}{\varepsilon_f} \, d\varepsilon_p \tag{11}$$

$$\varepsilon_f = \left\{ \frac{K}{c_2} \left[c_3 + \frac{\sqrt{3}}{2 - \sqrt{3}} (1 - c_3) \left(\sec \frac{\bar{\theta}\pi}{6} - 1 \right) \right] \times \left[\sqrt{\frac{1 + {c_1}^2}{3}} \cos \frac{\bar{\theta}\pi}{6} + c_1 \left(\eta + \frac{1}{3} \sin \frac{\bar{\theta}\pi}{6} \right) \right] \right\}^{-\frac{1}{n}} \tag{12}$$

where η is the stress triaxiality; $\bar{\theta}$ is the normalised Lode angle; and c_1, c_2 and c_3 are the MMC model parameters.

For the ease of calibration and for obtaining a physical sense of the effect of changes in the paramaters, the MMC parameters are normalised and expressed as C_1, C_2 and C_3, in the units of strains, as shown in Eqs. 13 to 16:

$$C_1 = \left(\frac{c_2}{c_3 K Z} \right)^{\frac{1}{n}} \tag{13}$$

$$C_2 = \left(\frac{2c_2}{K}\right)^{\frac{1}{n}} \tag{14}$$

$$C_3 = \left(\frac{\sqrt{3}c_2}{Kc_3}\right)^{\frac{1}{n}} \tag{15}$$

where Z is given by:

$$Z = \sqrt{\frac{1 + {c_1}^2}{3}} + 2.5c_1 \tag{16}$$

In the triaxiality-independent instance ($c_1 = 0$) of the MMC strain locus, C_1 and C_3 are both equal to the minimum strain in the locus, occurring at $\bar{\theta} = 0$, and C_2 is equal to the maximum strain in the locus, occurring at $\bar{\theta} = \pm 1$. Furthermore, C_1 is always equal to the value of the fracture strain for ($\eta = 2.5$, $\bar{\theta} = 0$), the perfectly plastic, plane-strain solution for the stress state at a crack tip, and the smaller C_1 is than C_3, the greater the triaxiality dependence.

A cut-off for the negative-triaxiality damage initiation strains is implemented numerically at $\eta = -1/3$ (Bao and Wierzbicki, 2005) by additionally increasing the damage initiation strain ε_f gradually towards infinity as η drops below $-1/3$. For the purpose of numerical convergence in the solution of the yield function (Eq. 1), the ε_f for $\eta \geq 3.5$ is kept constant at its value when $\eta = 3.5$. Such values of η typically only occur when the element is already highly damaged and degraded, so this approximation is not expected to change the solution.

As mentioned, the main purpose of this study is to find relationships that provide estimated calibrated damage parameters suitable for modelling fracture toughness in SENB simulations given only material certificate data, simplifying the conventionally tedious calibration procedure to facilitate the use of damage mechanics modelling in design considerations and parametric investigations of fracture toughness. Using experiments on an AH36 and an S690 steel, Wong and Walters (2025) have shown that the assumption of triaxiality independence, together with the aforementioned understanding of the correlation of D_c to the steel type and the assumption of linear degradation ($m = 1$), performs well in reducing the number of damage calibration parameters for weakly-triaxiality-dependent steels to only two (C_2 and C_3) while simulating the responses of the tensile, Charpy and SENB tests well. This is effectively a capitalisation of the weak triaxiality dependence of the steels in the medium-to-high triaxiality range, which is the range experienced in the tensile test as it necks and in the crack planes of the Charpy and SENB tests. A damage locus that is described by two parameters can be calibrated using only two types of tests, given that they cover distinct stress states which are in the stress-state range of interest, and material certificates provide the results of two such test in the form of the fracture elongation A and the Charpy energy C_v. Furthermore, it was observed that for key portions of the behaviour in the SENB and Charpy tests, namely well beyond the occurrence of the critical CTOD and up to 70 % of the dissipation of C_v, the stress states in the Charpy and SENB are very similar, being determined by extensive tunnelling behaviour with little or no slant fracture. Due to this, a calibration based on the Charpy tests provides a similar range of stress states as is provided by the calibration to a CTOD test (Wong and Walters, 2025). In light of this, this study derives calibration relationships between the damage parameters (C_2 and C_3) and properties obtained from the Charpy test (C_v) and the tensile test (A and σ_y/σ_u).

RELATIONSHIP BETWEEN MATERIAL CERTIFICATE DATA AND DAMAGE PARAMETERS

A parametric study varying the σ_y/σ_u and the key damage calibration parameters (C_2 and C_3) of the aforementioned material model in finite-element simulations of the Charpy and tensile test is performed in order to obtain sets of material certificate values with their corresponding damage parameters. For each (σ_y/σ_u, C_2, C_3) combination, both the Charpy and the tensile tests are simulated and then postprocessed to obtain the A and C_v. This allows the subsequent deduction of the relationship between (C_2, C_3) and (A, C_v, σ_y/σ_u) using regression analysis of the numerical results.

A is taken to be the engineering strain when the force first drops below zero, which has been found Wong and Walters (2025) to give a sufficiently close approximation of the value based on the standard definition (ISO, 2019) of summing the length of the broken gauge section and dividing the sum by the original gauge length. C_v is taken to be the total kinetic energy lost from the striker by the time the force has become stable around zero.

Parametric study

The simulations are performed in Abaqus Explicit (2022) with the use of a user-defined material subroutine for the implementation of the material model. Eight-noded linear solid elements with reduced integration and hourglass control (C3D8R) are used. As a result of a mesh sensitivity study, elements with characteristic sizes l_c of 0.12 mm and 0.06 mm, respectively, were used in the fracture zones of the tensile and Charpy tests, where l_c is the cube root of the volume of an undeformed element. Mass scaling was applied to the Charpy and tensile test to decrease the computational time. In the simulations of the quasi-static tensile tests, the mass was increased by a factor of 1×10^9, and the kinetic energy was checked to be less than 1 % of the total internal energy, except for the beginning of the simulation when the load application boundary accelerates to the quasi-static testing velocity. In the simulations of the dynamic Charpy tests, the mass was increased by a factor of 25, a value which is seen to produce a negligible difference in C_v in a previous mass scaling factor sensitivity study (Wong and Walters, 2024). The coefficient of friction between contact surfaces in the Charpy simulations was assumed to be 0.15.

Parametric space selection. Table 1 gives the σ_y/σ_u values that are considered in the parametric study. Although variation in the σ_y/σ_u is seen for steels with the same grade and the same σ_y, a higher σ_y is generally accompanied by a higher σ_y/σ_u. Therefore, the σ_y/σ_u is here made to vary with the σ_y in order to reduce the size of the parametric space while reflecting the general trend. Including a numerical dataset with varying σ_y/σ_u for fixed σ_y would shed further light on the separate effects of σ_y/σ_u and σ_y, but is outside the scope of this already computationally expensive study. It is also worth noting that, because of the range of σ_y/σ_u considered and the use of Eqs. 4 and 5, ε_{sh} and ε_u are assumed to be constant in this study. For each σ_y/σ_u, a series of simulations are run, using all the combination pairs of C_2 and C_3 values that can be made from [0.4, 2.6, 5.1, 7.6] and [0.4, 0.7, 1], respectively, with the exception that C_2 is set to equal C_3 in pairs where $C_2 < C_3$, since $C_2 < C_3$ does not align with experimental observations (see descriptions of Eqs. 14 and 15 above).

Table 1 Range of σ_y and σ_y/σ_u considered.

σ_y [MPa]	730	750	770	810	850
σ_y/σ_u [-]	0.92	0.93	0.94	0.96	0.97

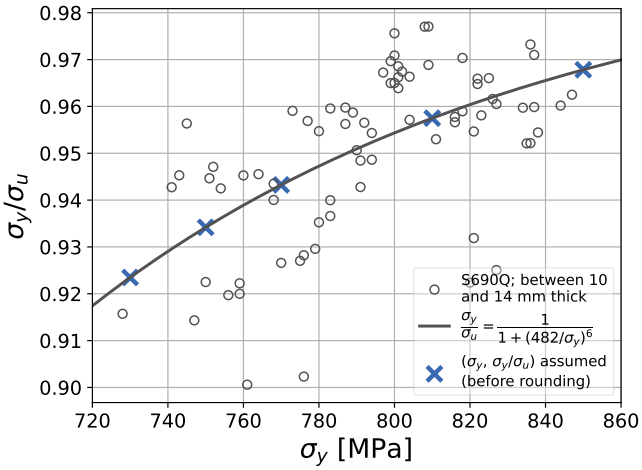

Fig. 2 σ_y/σ_u and σ_y assumed in the parametric study, based on fit to database.

The values chosen for σ_y and σ_y/σ_u are based on the database of material certificates provided by Huisman, from which 77 steels are used to form a parametric space, by discretising the σ_y domain into intervals, and taking the σ_y/σ_u predicted by a least-squares fit to these 77 steels, as shown in Fig. 2. The dataset of 77 steels is a result of the following filtering criteria applied to the database. First, only steels with the equivalent grades of StE690 and S690Q (CEN, 2019), which have the same minimum toughness standard, are included in the dataset. Second, only steels with a thickness between 10 and 14 mm were included in the dataset. In the tensile test simulations, the steel is assumed to be 12 mm and modelled with a standard (IACS, 2023) 25 mm width and proportional gauge length. The relatively small range of thicknesses in the dataset, centred around the value assumed in the simulations, is used so that more materials are included in the dataset while limiting any potential thickness effects that might exist despite the proportionality of the specimens (ASTM, 2024). Finally, only steels for which all the three C_v repetitions reported on the material certificate were larger than 100 J, and for which all three repetitions did not differ from each other by more than 50 J, were included in the dataset. This is to ensure that the Charpy tests considered in the dataset involved fully ductile behaviour even though these tests performed at −20 °C according to the corresponding material standard (CEN, 2019), since the simulations do not account for any transition to unstable cleavage fracture.

Charpy testing temperature assumed in the parametric study. The tensile tests, which are used to deduce the parameters describing the plastic strain-hardening behaviour assumed in the Charpy and tensile simulations, were performed at ambient temperature, while the Charpy tests were performed at −20 °C. The temperature affects the plastic flow stress of materials, but this temperature difference of −40 °C could be expected to make a relatively small difference in the flow stress (Yan et al., 2014). To ascertain the significance of this difference, Charpy simulations accounting for temperatures of −20 °C and −60 °C were additionally performed for the calibrated S690QL steel investigated in Wong and Walters (2025), which was one of the materials for which detailed experimental comparisons were carried out as part of the validation of the present material modelling approach. Since the Johnson-Cook-based model described above (Eq. 7) is suitable only for thermal softening at temperatures above room temperature, the effect of the lower temperature is included here by directly modifying the entire plastic strain-hardening curve according to the BS7910 (BSI, 2019) equation recommended for assessment temperatures below room temperature and above −196 °C, given the room temperature yield strength:

$$\sigma_{y,cold} = \sigma_{y,room} + \frac{10^5}{491 + 1.8\Theta} - 189 \tag{17}$$

where $\sigma_{y,cold}$ [MPa] is the estimated yield stress at low temperature, $\sigma_{y,room}$ [MPa] is the yield stress at room temperature, and Θ [°C] is the temperature.

For simplicity, this relationship is assumed to be applicable directly to the true plastic strain hardening stress $\bar{\sigma}$ (Eq. 2), such that the temperatures of −20 °C and −60 °C result in a uniform increase to the $\bar{\sigma}$ of 31 MPa and 72 MPa, respectively, for all ε_p. This assumption of uniform increase is in line with the observed effect of lower temperatures on the shape of the stress-strain curves as seen in Yan et al. (2014). The other material parameters, including the thermal softening parameters, are kept the same (Table 2), and the simulations start at room temperature with the uniformly increased plastic strain-hardening curve due to the lower temperature, such that the thermal softening model (Eq. 7) is assumed to act based on the temperature difference relative to the starting temperature.

Table 2 Calibrated material parameter values from Wong and Walters (2025) for an S690QL steel, used in combination with Eq. 17 for the low-temperature ductile simulations.

(a) Plasticity and damage.

		S690QL
σ_y	[MPa]	836
$\varepsilon_{sh,p}$	[-]	0.0438
ε_0	[-]	0.0413
K	[MPa]	984.1
n	[-]	0.0192
C_1	[-]	0.47
C_2	[-]	8.50
C_3	[-]	0.47
m	[-]	1
D_c	[-]	1.3

(b) Rate dependence, thermal effects and elasticity.

		S690QL
C	[s^{-1}]	40524.5
q	[-]	3.3
$\dot{\varepsilon}_{p,uni}$	[s^{-1}]	0.00025
$\dot{\varepsilon}_{p0}$	[s^{-1}]	0.00025
Θ_m	[°C]	1527
Θ_r	[°C]	20
m_x	[-]	1.071
c	[$J\,kg^{-1}\,°C^{-1}$]	452
E	[MPa]	206064
ν	[-]	0.3

The simulation results (Fig. 3 and Table 3) indicate that a testing temperature of −20 °C, and the associated 31 MPa increase in flow stress relative to room temperature conditions, makes a negligible difference to both the Charpy force-displacement curve and the Charpy energy, assuming that the Charpy test behaviour is in the fully ductile regime. In contrast, the temperature rise around the notch due to adiabatic effects, which could be as much as 350 °C (Tanguy et al., 2005), would lead to a 20 % decrease in the flow stress, given the present thermal softening parameters (Table 2). Therefore, the Charpy simulations in the parametric study, which do take the thermal softening effects into account, are performed assuming room temperature plastic strain-hardening properties, although the Charpy tests were performed at −20 °C.

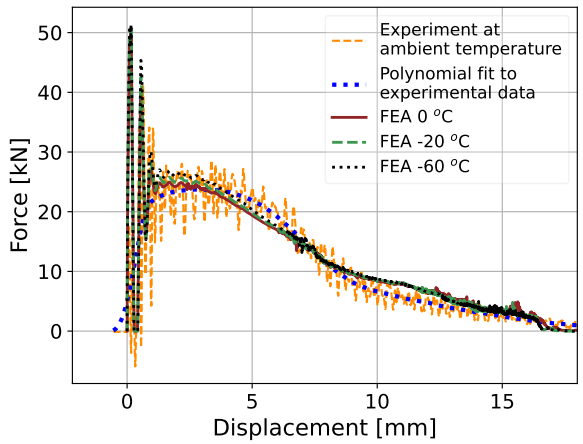

Fig. 3 Charpy simulations of S690QL steel at −60 °C, −20 °C and 20 °C.

Table 3 Charpy energy values in simulations with flow stress modified to account for lower temperatures.

		Test	Simulations		
Θ	[°C]	~ 20	−60	−20	20
C_v	[J]	204.2	224.7	219.6	217.1

Regression of A and C_v on C_2, C_3 and σ_y/σ_u

The results of the parametric runs, together with a fitted relationship based on least-squares regression, are plotted in Figs. 4 to 7. The proposed regression model is given in Eq. 18 and is a result of fitting different trial models based on the trends observed in the data and choosing the one that best reflect the trends.

$$\begin{cases} C_v(C_2, C_3, \dfrac{\sigma_y}{\sigma_u}) = P_1 P_2^{\left(\frac{\sigma_y}{\sigma_u}-1\right)} {C_2}^{P_3} + P_4 P_5^{\left(\frac{\sigma_y}{\sigma_u}-1\right)} \dfrac{\sigma_y}{\sigma_u} {C_3}^{P_6} \\ \qquad\qquad + P_7 P_8^{\left(\frac{\sigma_y}{\sigma_u}-1\right)} {C_2}^{P_9} {C_3}^{P_{10}} \\ A(C_2, C_3) = Q_1 {C_2}^{Q_2} + Q_3 {C_3}^{Q_4} + Q_5 {C_2}^{Q_6} {C_3}^{Q_7} \end{cases} \tag{18}$$

where P_i and Q_i are the fitting parameters, as shown in Table 4, together with their units as determined by dimensional analysis.

Table 4 Fitted calibration parameters.

(a) P_i parameters.

i	units	P_i
1	[J]	−1101.5
2	[-]	29.352
3	[-]	0.070324
4	[J]	−7611.0
5	[-]	6.7044
6	[-]	0.40209
7	[J]	9100.1
8	[-]	19.509
9	[-]	0.014450
10	[-]	0.36260

(b) Q_i parameters.

i	units	Q_i
1	[-]	5.0436
2	[-]	−0.46857
3	[-]	0.21566
4	[-]	0.23271
5	[-]	5.1007
6	[-]	0.46790
7	[-]	0.0041338

The data points in Figs. 4b, 5b and 6b show that σ_y/σ_u has no appreciable effect on A. Because σ_y/σ_u is assumed to vary monotonically with σ_y, this also implies that σ_y has little effect on A. The tiny variations seen in A with respect to changes in σ_y/σ_u seen in these plots appear as scatter with no consistent trend. Hence, it is assumed that σ_y/σ_u has no effect on A in this regime and does not appear as a variable in the equation for A. From Figs. 4 and 5, both A and C_v appear to have a power-law relation with respect to C_2 and C_3, although this is relatively weak between A and C_3, especially when C_2 is high. Additionally, Fig. 6a suggests that C_v has an exponential dependence on σ_y/σ_u. The proposed nature of the dependencies between the individual variables are summarised in Table 5. These determine the form of constituent terms chosen in the Eq. 18, i.e. $P_i^{\left(\frac{\sigma_y}{\sigma_u}-1\right)}$ for exponential relations and $P_i {C_i}^{P_j}$ or $Q_i {C_i}^{Q_j}$ for power relations.

Table 5 Dependencies of C_v and A on C_2, C_3 and σ_y/σ_u.

	C_2 [-]	C_3 [-]	σ_y/σ_u [-]
C_v [J]	Power	Power	Exponential
A [-]	Power	Power	None

The data points in Figs. 4 to 6 also reveal information about the coupling between the plasticity parameter σ_y/σ_u and the damage parameters C_2 and C_3. It can be seen that changes in C_3 nonlinearly affects the way C_v is related to C_2 (Fig. 4a) and changes in C_2 nonlinearly affects the way C_v is related to C_3 (Fig. 5a). The same can be said of the relationship between A, C_2 and C_3. Therefore, the terms $P_i {C_2}^{P_j} {C_3}^{P_k}$ and $Q_i {C_2}^{Q_j} {C_3}^{Q_k}$ are included in the equation for C_v and A, respectively. From Fig. 4a, 5a and 6a, the coupling effect is also seen to act between σ_y/σ_u, C_2 and C_3. So, multiplicative terms between $P_i^{\left(\frac{\sigma_y}{\sigma_u}-1\right)}$, $P_i {C_2}^{P_j}$ and $P_i {C_3}^{P_j}$ are used in the equation for C_v.

Since C_2 and C_3 are normalised parameters representing, respectively, the maximum (at $\bar{\theta} = \pm 1$) and minimum (at $\bar{\theta} = 0$) strains in the triaxiality-independent strain-based MMC damage locus (see section on Damage above), some physical sense could be derived from these findings.

From Figs. 5 and 7, the effect of C_3 is stronger on C_v than on A. This could be related to how the tunneling effects in the Charpy test, which have been shown to have a dominant effect in the behaviour (Wong and Walters, 2025), begin at mid-thickness in the specimen, where $\bar{\theta} = 0$. In contrast, $\bar{\theta}$ in the tensile test starts at 1 and gradually drops as necking occurs. The difference in the proportion of effects caused by C_2 and C_3 on C_v and A sheds light on the role played by each damage parameter in the process of calibration. While it is obvious that materials with high A and C_v are characterised by both high C_2 and high C_3, these results reveal information about the trends that characterise materials with high notch toughness C_v but low uniaxial-test fracture elongation A. Fig. 7 suggests that for a material with triaxiality-independent damage behaviour, the combination of high C_v and low A is characterised by combinations of high damage initiation strains at $\bar{\theta} = 0$ and low damage initiation strains at $\bar{\theta} = 1$. Conversely, a combination of low notch toughness and high uniaxial-test fracture elongation is characterised by low C_2 and high C_3.

It is also worth noting that the effect of C_2 (the maximum strain of the damage initiation locus) on C_v, which was identified as being very weak in previous work by the present authors (Wong and Walters, 2024), could in fact become significant if the variations in C_2 become very

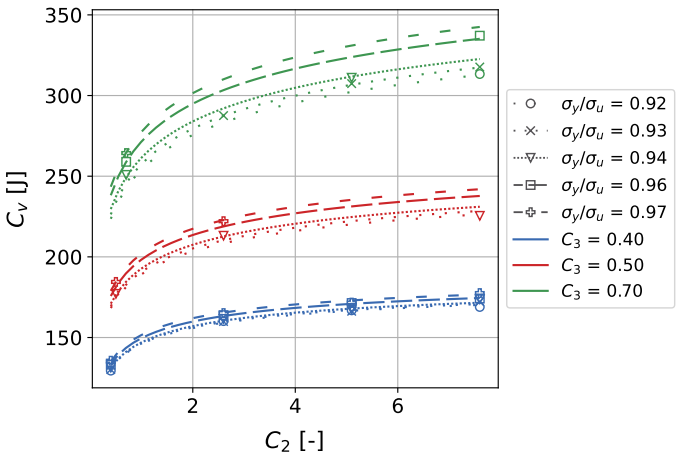

(a) C_v against C_2

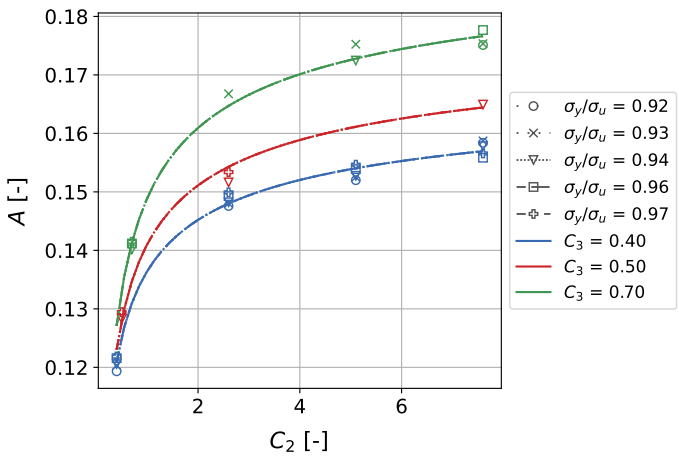

(b) A against C_2

Fig. 4 C_v and A against C_2 from the parametric simulations.

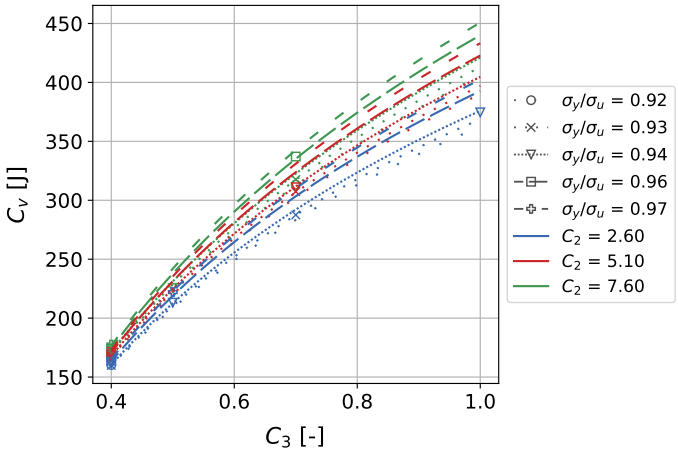

(a) C_v against C_3

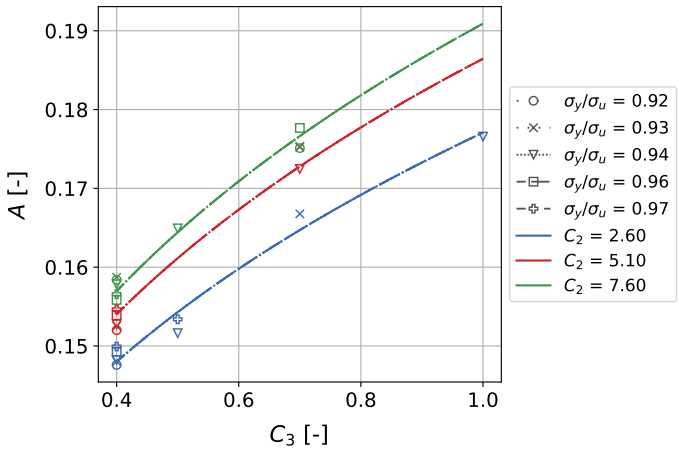

(b) A against C_3

Fig. 5 C_v and A against C_3 from the parametric simulations.

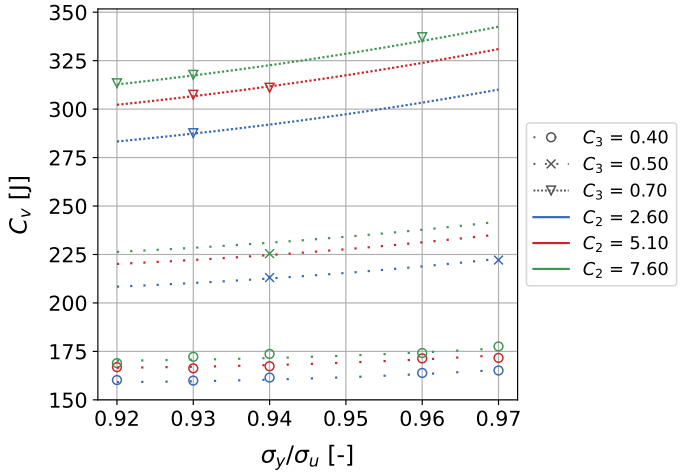

(a) C_v against σ_y/σ_u

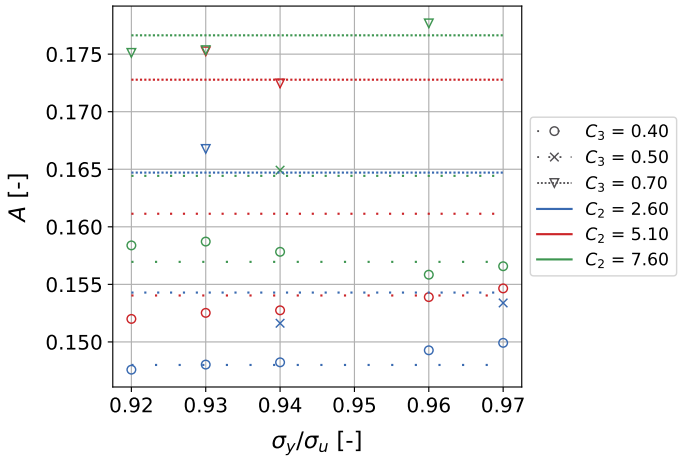

(b) A against σ_y/σ_u

Fig. 6 C_v and A against σ_y/σ_u from the parametric simulations.

large (Fig. 4a).

Finally, given a set of material certificate values for a steel within the range of the parametric study, Eq. 18 can be solved numerically to find an estimation of the calibrated damage parameters C_2 and C_3. Naturally, the range of A and C_v for which solutions exists has its bounds, as can be guessed from the surfaces shown in Fig. 7. Furthermore, the solution should not involve extrapolation beyond the range investigated by the parametric study. Figs. 8 and 9 show examples involving ranges for which the solution of Eq. 18 exists within the investigated range. Comparing Figs. 8 and 9, it is evident that A has a far stronger effect on the correlation between C_2 and C_v and the correlation between C_3 and C_v than does σ_y/σ_u, even when the coupling between plasticity and damage has been accounted for. Since C_2 and C_3 represent the maximum and minimum damage initiation strains in the triaxiality-independent instance of the strain-based MMC, they are strongly correlated to ductile fracture behaviour and toughness. This implies that differences in σ_y/σ_u can be expected to have a relatively small effect on ductile fracture behaviour, given fixed values of C_v and A. On the other hand, C_v and A are much more important parameters for ductile fracture. While the correlation between C_v and fracture toughness is well known (Wallin, 2001; BSI, 2019), variations in A and σ_y/σ_u have not been accounted for in these correlations. The small influence of σ_y/σ_u relative to that of A observed here also calls into question the suitability of σ_y/σ_u as an indirect indicator of local ductility in design standards and rules (Wong and Walters, 2021), on which the recent literature still lacks consensus, with some suggesting that a higher σ_y/σ_u improves fracture resistance (Feldmann and Schaffrath, 2017; Feldmann et al., 2020) and others suggesting the contrary (Nonn et al., 2018; Lu et al., 2015). More conclusive insight into the role of the A and σ_y/σ_u remains to be uncovered through the consideration of fracture toughness testing and damage mechanics simulations of such tests in view of the present findings.

CONCLUSIONS AND RECOMMENDATIONS

By performing a parametric study with regression analysis on a previously validated damage-plasticity model accounting for rate dependence, thermal effects and damage softening, correlations between the damage mechanics parameters describing the damage initiation locus and material certificate properties have been proposed for S690Q steels with yield strengths between 730 MPa and 850 MPa. These correlations have been developed for the purpose of modelling tensile, Charpy and SENB fracture toughness tests for a specific group of steels considered, namely S690Q steels with weak triaxiality dependence in the medium-to-high triaxiality range. In this sense, the correlations act as a tool to greatly simplify the conventionally tedious calibration procedure, so that damage mechanics modelling can be used in subsequent parametric investigations of SENB testing and design considerations concerning fracture toughness.

In a broader sense, the correlations give insight into the trends and relative importance of the plasticity and damage parameters in relation to the variations in A and C_v. By relating the engineering properties obtained from Charpy and tensile specimens, which are subject to known stress states at key locations, to the strains in stress-state-dependent damage initiation locus, physical insight is obtained regarding the role of the normalised damage parameters, revealing which combinations of maximum and minimum strains in the Lode-dependent, triaxiality-independent damage locus might lead to combinations of high C_v and low A or of low C_v and high A. Such information is useful both for understanding how plasticity parameters are related to fracture toughness and for the future calibration of similar materials. The correlations also give information on how the damage and plasticity parameters and coupled in their effect on C_v and A.

It is seen that σ_y/σ_u has a small effect on the correlations between notch toughness and damage initiation strains while A has a significantly larger effect. Since the damage initiation strains are directly correlated to the fracture behaviour, this suggests that the existing correlations between C_v and fracture toughness (e.g. C_v to CTOD conversions), which have not taken the effect of variations in A and σ_y/σ_u into account, should be reconsidered in light of these effects, especially that of A, due to its strong correlation with the damage initiation strains. This also suggests that the σ_y/σ_u ratio, which is used in current rules and standards as an indirect indicator for the local ductility that can be provided by a material at a structural detail against ductile fracture, might actually be ineffective for this purpose due to its small influence, a point which remains to be ascertained through further study of fracture toughness testing and simulation in light of the present findings.

Finally, it is worth noting that this study adopts the assumption of a deterministic correlation between σ_y/σ_u and σ_y based on the trend observed in the database of materials considered, one that is observed in structural steels in general. However, scatter in σ_y/σ_u for given σ_y naturally exists, and further considering variations in σ_y/σ_u independently of σ_y could reveal more nuanced information about the effect of the plasticity parameters. Although it is unlikely that such a consideration would make large quantitative changes in the correlations, since the effect of a varying σ_y/σ_u presently observed is already small, it might better reveal trends and differences in the dependence of C_v and A on strength and strain hardening separately.

ACKNOWLEDGMENTS

The authors gratefully acknowledge the joint funding provided by the Bureau Veritas Marine & Offshore SAS, Damen Schelde Naval Shipbuilding, Huisman, Lloyd's Register EMEA, POSCO and the Topconsortia voor Kennis en Innovatie (TKI). The authors also thank Huisman for providing the material certificate database used in the study.

REFERENCES

Alabi, A. A., Moore, P. L., Wrobel, L. C., Campbell, J. C. and He, W. (2018). Tensile behaviour of S690QL and S960QL under high strain rate, *Journal of Constructional Steel Research* **150**: 570–580.

Algarni, M., Bai, Y. and Choi, Y. (2015). A study of Inconel 718 dependency on stress triaxiality and Lode angle in plastic deformation and ductile fracture, *Engineering Fracture Mechanics* **147**: 140–157.

ASTM (American Society for Testing and Materials) (2024). *E8/E8M - 24 Standard Test Methods for Tension Testing of Metallic Materials*, ASTM, West Conshohocken.

Bai, Y. and Wierzbicki, T. (2010). Application of extended Mohr–Coulomb criterion to ductile fracture, *International Journal of Fracture* **161**(1): 1–20.

Banabic, D., Aretz, H., Paraianu, L. and Jurco, P. (2005). Application of various FLD modelling approaches, *Modelling and Simulation in Materials Science and Engineering* **13**(5): 759–769.

Bao, Y. and Wierzbicki, T. (2005). On the cut-off value of negative triaxiality for fracture, *Engineering Fracture Mechanics* **72**(7): 1049–1069.

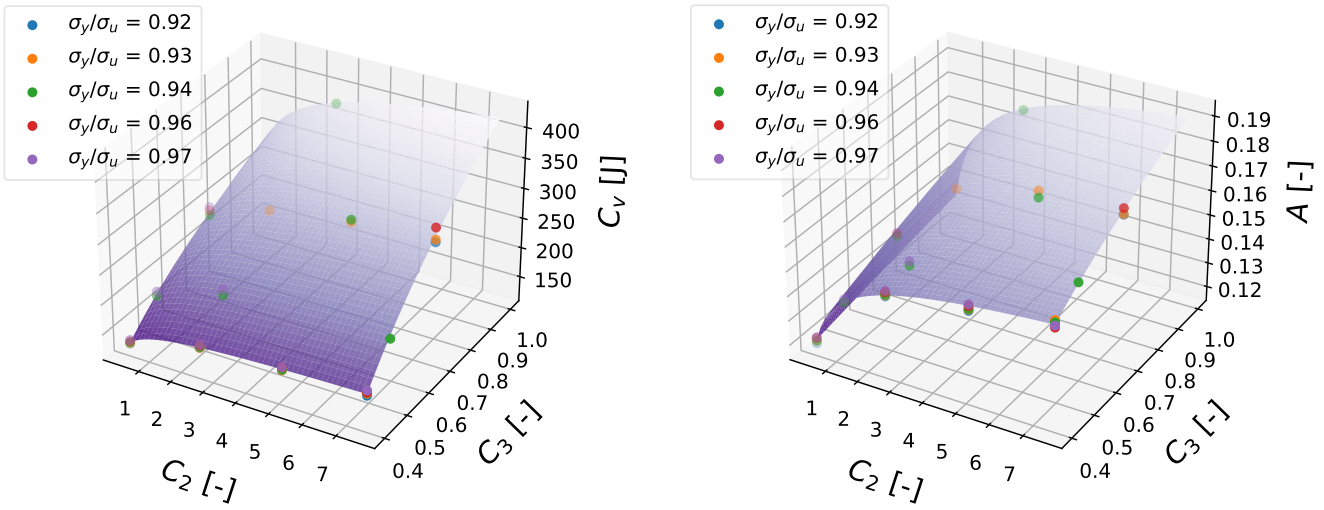

(a) C_v against C_2 and C_3 (b) A against C_2 and C_3

Fig. 7 C_v and A against C_2 and C_3 from the parametric simulations together with fitted surface (using $\sigma_y/\sigma_u = 0.93$ as an example).

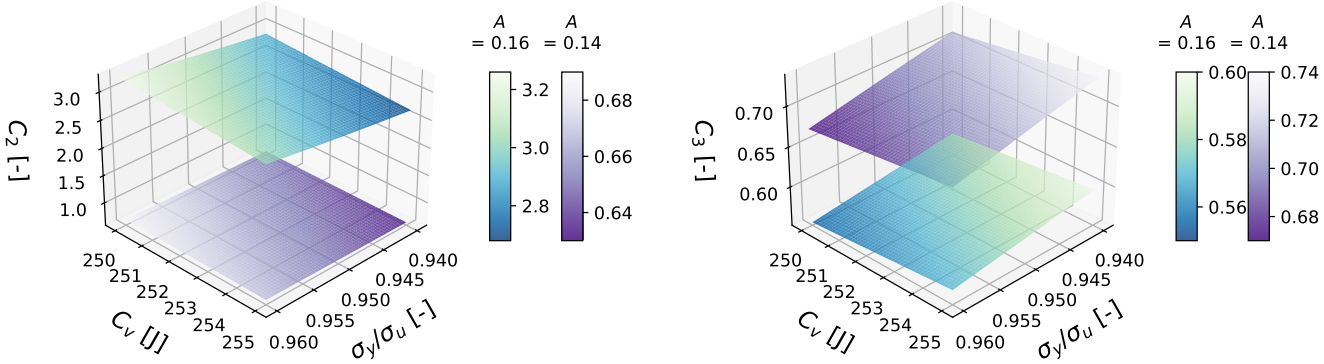

(a) C_2 against C_v and A (b) C_3 against C_v and A

Fig. 8 C_2 and C_3 against C_v and A obtained from solving Eq. 18.

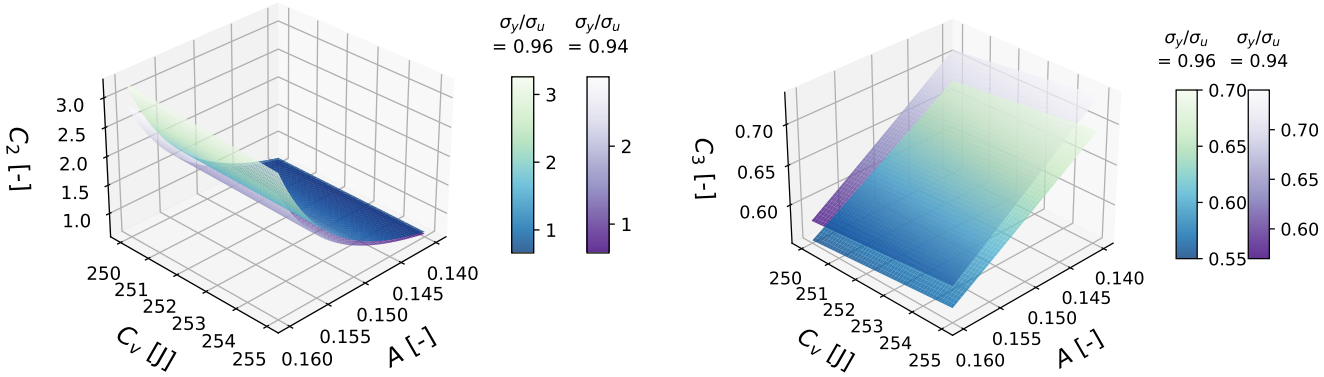

(a) C_2 against C_v and σ_y/σ_u (b) C_3 against C_v and σ_y/σ_u

Fig. 9 C_2 and C_3 against C_2 and C_3 obtained from solving Eq. 18.

Besseling, J. F. and van der Giessen, E. (1994). *Mathematical Modelling of Inelastic Deformation*.

BSI (British Standards Institution) (2019). *BS 7910 Guide to methods for assessing the acceptability of flaws in metallic structures*, BSI.

Cao, T. S. (2015). Models for ductile damage and fracture prediction in cold bulk metal forming processes: a review, *International Journal of Material Forming* **10**(2): 139–171.

CEN (European Committee for Standardization) (2019). *EN 10025-6 Hot rolled products of structural steels - Part 6: Technical delivery conditions for flat products of high yield strength structural steels in the quenched and tempered condition*, CEN, Brussels.

Chen, A., Zhang, P., Chen, B., Li, Y. and Xing, J. (2023). A new ductile fracture model for Q460C high-strength structural steel under monotonic loading: Experimental and numerical investigation, *Engineering Fracture Mechanics* **288**.

Clausing, D. P. (1970). Effect of plastic strain state on ductility and toughness, *International Journal of Fracture Mechanics* **6**(1): 71–85.

Considère, A. (1885). Mémoire sur l'emploi du fer et de l'acier, *Annales des Ponts et Chaussées* **9**: 574–775.

Cowper, G. R. and Symonds, P. S. (1957). Strain hardening and strain-rate effects in the impact loading of cantilever beams, *Technical Report no. 28*, Office of Naval Research.

Dey, S., Borvik, T., Hopperstad, O. S., Leinum, J. R. and Langseth, M. (2004). The effect of target strength on the perforation of steel plates using three different projectile nose shapes, *International Journal of Impact Engineering* **30**(8-9): 1005–1038.

Dong, J., Elchalakani, M., Li, D., Xiong, G. and Yang, B. (2022). Dynamic hardening behavior and ductile fracture of high-strength steel at intermediate strain rates, *Journal of Structural Engineering* **148**(9).

DS Simulia (Dassault Systèmes Simulia) (2022). ABAQUS 2022. Commercial Finite Element Software.

Feldmann, M. and Schaffrath, S. (2017). Assessing the net section resistance and ductility requirements of en 1993-1-1 and en 1993-1-12, *Steel Construction* **10**(4): 354–364.

Feldmann, M., Schaffrath, S. and Sandro, C. (2020). Draft: Background document to Eurocode 3 EN 1993 – part 1-10: Material toughness - approach for upper-shelf toughness requirements for the design of steel structures based on damage mechanics, *Technical report*, Institute of Steel Construction RWTH Aachen University.

Huo, J.-S., Zeng, X. and Wang, H.-T. (2022). Tensile behaviour of TMCP Q690D high-strength structural steel at strain rates from 0.00025 to 760 s-1, *Advanced Steel Construction* **18**(1): 488–494.

IACS (International Association of Classification Societies) (2023). *IACS UR W Requirements concerning material and welding*, IACS.

ISO (International Organization for Standardization) (2019). *ISO 6892-1 Metallic materials - Tensile testing - Part 1: Method of test at room temperature*, ISO, Geneva.

Johnson, G. R. and Cook, W. H. (1985). Fracture characteristics of three metals subjected to various strains, strain rates, temperatures and pressures, *Engineering Fracture Mechanics* **21**(1): 31–48.

Li, Y. and Wierzbicki, T. (2010). Prediction of plane strain fracture of AHSS sheets with post-initiation softening, *International Journal of Solids and Structures* **47**(17): 2316–2327.

Lu, C., Michal, G. and Venton, P. (2015). A new fracture velocity model for high grade gas pipelines, *20th Joint Technical Meeting on Pipeline Research*.

Meyers, M. A. (1994). *Dynamic Behavior of Materials*, John Wiley & Sons Inc.

Mohr, D. and Marcadet, S. J. (2015). Micromechanically-motivated phenomenological hosford–coulomb model for predicting ductile fracture initiation at low stress triaxialities, *International Journal of Solids and Structures* **67-68**: 40–55.

Nonn, A., Paredes, M., Keim, V. and Wierzbicki, T. (2018). Comparison of fracture models to quantify the effects of material plasticity on the ductile fracture propagation in pipelines, *2018 12th International Pipeline Conference*, Vol. Volume 3: Operations, Monitoring, and Maintenance; Materials and Joining, ASME.

Sakonder, C., Xue, L., Paredes, M., Savioli, R. and Sarzosa, D. F. B. (2022). Directional dependence of critical axial strain in X65 pipeline steel subject to combined internal pressure and bending loading, *International Journal of Pressure Vessels and Piping* **196**.

Sarzosa, D. F. B., Paredes, M., Savioli, R., Ruggieri, C., Leite, L. G. T. S., da Silva, N. S. and Garmbis, A. G. (2022). Experimental and numerical study on the ductile fracture response of X65 girth-welded joint made of Inconel 625 alloy, *Theoretical and Applied Fracture Mechanics* **121**.

Seo, K.-W., Kim, J.-Y., Kim, Y.-J. and Kim, K.-S. (2024). Finite element ductile fracture simulation of Charpy and drop weight tear tests for API X52, *Theoretical and Applied Fracture Mechanics* **133**.

Swift, H. W. (1952). Plastic instability under plane stress, *Journal of the Mechanics and Physics of Solids* **1**: 1–16.

Tanguy, B., Besson, J., Piques, R. and Pineau, A. (2005). Ductile to brittle transition of an A508 steel characterized by charpy impact test, *Engineering Fracture Mechanics* **72**(3): 413–434.

Taylor, G. I. and Quinney, H. (1933). The latent energy remaining in a metal after cold working, *Proceedings of the Royal Society of London. Series A, Containing Papers of a Mathematical and Physical Character* **143**(849): 307–326.

Wallin, K. (2001). Low-cost J-R curve estimation based on CVN upper shelf energy, *Fatigue & Fracture of Engineering Materials & Structures* **24**(8): 537–549.

Wang, W. M., Sluys, L. J. and de Borst, R. (1997). Viscoplasticity for instabilities due to strain softening and strain-rate softening, *International Journal for Numerical Methods in Engineering* **40**(20): 3839–3864.

Wong, W. J. and Walters, C. L. (2021). Failure modes and rules related to the yield-to-tensile strength ratio in steel structures, *ASME 2021 40th International Conference on Ocean, Offshore and Arctic Engineering (OMAE)*, ASME (The American Society of Mechanical Engineers).

Wong, W. J. and Walters, C. L. (2024). Effects of strain hardening and the Lode dependence of the fracture strain locus on slant fracture in Charpy V-notch impact testing, *ASME 2024 43rd International Conference on Ocean, Offshore and Arctic Engineering (OMAE)*, ASME (The American Society of Mechanical Engineers).

Wong, W. J. and Walters, C. L. (2025). Damage mechanics model for correlating notch toughness in Charpy impact tests with fracture toughness in cracked static fracture tests., *Manuscript*. Under review.

Xue, L. (2009). Stress based fracture envelope for damage plastic solids, *Engineering Fracture Mechanics* **76**(3): 419–438.

Xue, L. (2010). Localization conditions and diffused necking for damage plastic solids, *Engineering Fracture Mechanics* **77**(8): 1275–1297.

Yan, J.-B., Liew, J. Y. R., Zhang, M.-H. and Wang, J.-Y. (2014). Mechanical properties of normal strength mild steel and high strength steel S690 in low temperature relevant to arctic environment, *Materials & Design* **61**: 150–159.

Yang, X., Yang, H., Lai, Z. and Zhang, S. (2020). Dynamic tensile behavior of S690 high-strength structural steel at intermediate strain rates, *Journal of Constructional Steel Research* **168**.

Yang, X., Yang, H. and Zhang, S. (2019). Rate-dependent constitutive models of S690 high-strength structural steel, *Construction and Building Materials* **198**: 597–607.

Yun, X. and Gardner, L. (2017). Stress-strain curves for hot-rolled steels, *Journal of Constructional Steel Research* **133**: 36–46.